Optimal Endurance Race Strategies for a Fully Electric Race Car Under Thermal Constraints

Jorn van Kampen, Thomas Herrmann, Theo Hofman, and Mauro Salazar

***Abstract*— This article presents a bi-level optimization framework to compute the offline maximum-distance race strategies for a fully electric endurance race car, whilst accounting for the low-level vehicle dynamics and the thermal limitations of the powertrain components. Thereby, the lower level computes the minimum-stint-time for a given charge time and stint length, whilst the upper level leverages that information to jointly optimize the stint length, charge time, and number of pit stops, in order to maximize the driven distance in the course of a fixed-time endurance race. Specifically, we first extend a convex lap time optimization framework to capture low-level vehicle dynamics and thermal models and use it to create a map linking the charge time and stint length to the achievable stint time. Second, we leverage the map to frame the maximum-race-distance problem as a mixed-integer second-order conic program that can be efficiently solved in a few seconds to the global optimum with off-the-shelf optimization algorithms. Finally, we showcase our framework for a simulated 6 h race around the Zandvoort circuit. Our results show that the optimal race strategy can involve partially charging the battery, and that, compared to the case where the stints are optimized for a fixed number of pit stops, jointly optimizing the stints and number of pit stops can significantly increase the driven distance and hence race performance by several laps.**

***Index Terms*— Electric vehicles, endurance racing, optimal control, optimization, race strategy.**

I. Introduction

THE electrification of race cars has been increasing in popularity over the last years, due to the advent of hybrid electric Formula 1 cars and Le Mans Hypercars, and battery electric vehicles in Formula E. In a setting where every millisecond counts, it is of paramount importance to make efficient use of the energy stored on-board via optimized energy management strategy (EMS), whilst respecting the thermal limits of the powertrain components. This problem is even more apparent for fully electric race cars, such as the vehicle shown in Fig. 1, where the available on-board energy is relatively small, compared to conventional race cars. Whereas fuel is the main energy source in conventional race cars, fully electric race cars rely on a less energy-dense battery that is typically integrated within the powertrain according to Fig. 2.

Fig. 1. InMotion's fully electric endurance race car [1].

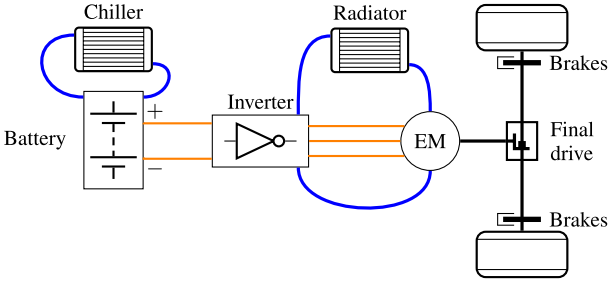

Fig. 2. Schematic overview of the electric endurance race car powertrain with the electrical connections highlighted in orange and cooling in blue. The battery is actively cooled by a refrigerant system, whereas the electric machine (EM) is cooled by a conventional radiator system.

In this context, the necessity of recharging the battery in the course of the race further complicates the problem, requiring race engineers to strike the best tradeoff between reducing energy consumptions and pit stops at the cost of lap time, or driving faster with more pit stops, whilst avoiding damage to the powertrain components by staying within the thermal limits. This conflict is particularly imminent in endurance racing, where the objective is to maximize the driven distance in a fixed amount of time, which can range up to 24 h [2]. In this setting, the car has to be strategically recharged during pit stops in order to maintain a competitive performance and maximize the distance driven. This calls for algorithms to compute the maximum-distance race strategies that provide the number of pit stops during the race, the number of laps driven per stint (referred to as stint lengths), and the charge time (which is directly correlated with charge energy),

Manuscript received 6 August 2023; accepted 7 November 2023. This work was supported in part by the NEON Research Project [Crossover Program which is (partly) financed by the Dutch Research Council (NWO)] under Grant 17628. Recommended by Associate Editor E. Hellström. *(Corresponding author: Jorn van Kampen.)*

Jorn van Kampen, Theo Hofman, and Mauro Salazar are with the Control Systems Technology Section, Department of Mechanical Engineering, Eindhoven University of Technology (TU/e), 5600 MB Eindhoven, The Netherlands (e-mail: j.h.e.v.kampen@tue.nl; t.hofman@tue.nl; m.r.u.salazar@tue.nl).

Thomas Herrmann is with the Institute of Automotive Technology, Department of Mechanical Engineering, Technical University of Munich (TUM), 80333 Munich, Germany (e-mail: thomas.herrmann@tum.de).

Color versions of one or more figures in this article are available at https://doi.org/10.1109/TCST.2023.3340793.

Digital Object Identifier 10.1109/TCST.2023.3340793

whilst accounting for the optimal in-stint strategy in terms of powertrain operation (PO). Thereby, the PO accounts for the thermal management of the powertrain components and for the battery energy management. Against this backdrop, this article presents a bi-level optimization framework to compute the maximum-distance race strategies with global optimality guarantees.

A. Related Literature

This work pertains to two main research streams: single-lap optimization of the EMSs jointly with the vehicle trajectory or for a given vehicle trajectory, and full-race optimization via simulations.

Several authors have optimized the minimum-lap-time racing line for a single lap using both direct and indirect optimization methods [3], [4], [5], [6], [7], [8], [9], [10], [11]. As opposed to these qualifying scenarios, racing scenarios are often additionally constrained by energy availability from either the fuel tank or the battery. To approach these racing conditions, some of these single-lap studies included a maximum energy consumption per lap [12], [13]. Similar approaches extend the minimum-lap-time problems to minimum-race-time problems. They consider temperature dynamics and optimize for multiple consecutive race laps to enable a variable amount of energy consumed per lap, yet formulate the optimization problem in the space domain for an a priori known number of laps [14], [15]. Finally, considering the racing line to be fixed, multilap EMSs are optimized, leveraging nonlinear optimization techniques [16] or artificial neural networks [17]. However, these papers lack global optimality guarantees.

Against this backdrop, assuming the racing line to be available in the form of a maximum speed profile, convex optimization has been successfully leveraged to compute the globally optimal EMSs for hybrid and fully electric race vehicles [18], [19], also including gear shift strategies [20], different transmission technologies [21], and thermal limitations [22]. Yet these methods are either focused on single-lap problems, not capturing pit stops or recharging processes, or they lack global optimality guarantees due to the use of iterative algorithms.

The second relevant research stream involves race simulations, in which entire races are optimized on a per lap basis [23], [24]. However, these studies mainly focus on optimal tire strategies by modeling their degradation as a lap time increase and do not capture the PO during a lap.

In conclusion, to the best of our knowledge, there are no methods specifically focusing on race strategies in endurance scenarios by which the single-stint operational strategies are jointly optimized together with the high-level stint planning and accounting for the thermal limits of the powertrain components.

B. Statement of Contributions

This article presents a bi-level mixed-integer convex optimization framework to efficiently compute the globally optimal maximum-distance endurance race strategies and

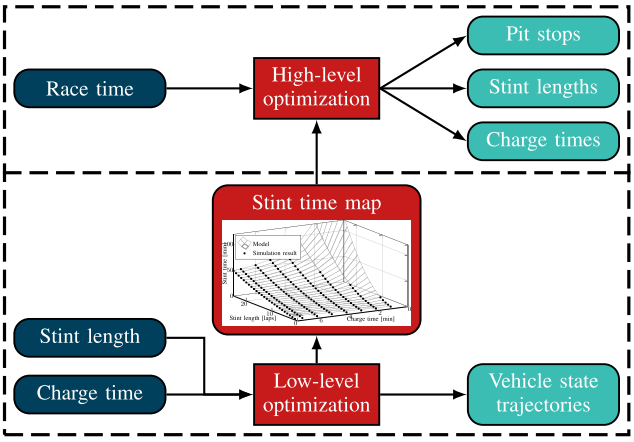

Fig. 3. Block diagram overview of the general approach to optimizing the race strategy. The low-level framework provides the state trajectories and minimum stint time for several combinations of stint length and charge time. The high-level framework optimizes the race strategy for a given race time, using the stint time data.

the corresponding PO in the individual stints, disregarding dynamic events such as overtaking maneuvers, safety car situations, and weather changes. In order to optimize the strategy over the complete race duration, we decompose an entire endurance race into separate stints and pit stops. Our low-level algorithm computes the optimal stint time for a given number of laps and the level of recharged battery energy. Subsequently, we fit the relationship between the stint length, the charged energy, and the achievable stint time as a second-order conic constraint, which we leverage in the high-level algorithm. Thereby, we frame the maximum-distance race problem as a mixed-integer second-order conic program, which jointly optimizes the stint length, the charge time, and the number of pit stops. The resulting problem can be rapidly solved with off-the-shelf numerical solvers with global optimality guarantees. This procedure is schematically visualized as a block diagram, shown in Fig. 3.

A preliminary version of this article was accepted for presentation at the 2022 European Control Conference, and selected for direct publication in a special issue of the European Journal of Control [25]. Whilst our previous study mainly focused on energy management, we now aim to more accurately represent an endurance racing scenario by accounting for the temperature dynamics of the powertrain components and for the vehicle dynamics. To this end, we include a more accurate battery loss model that captures the dependence on its energy and temperature and identify a method to model the battery and electric motor (EM) temperature dynamics in a convex form. Moreover, we directly include the vehicle dynamics in the low-level control problem by devising a convex framework in the form of a single-track model (shown in Fig. 4), so that we can better estimate the vehicle capabilities and no longer rely on a precomputed maximum speed profile. This way, the velocity of the vehicle is directly constrained in the optimization problem via the maximum tire forces. To account for these extensions, we reformulate the high-level control problem by decomposing the race into stints followed by pit stops, instead of stints being preceded by pit stops, and

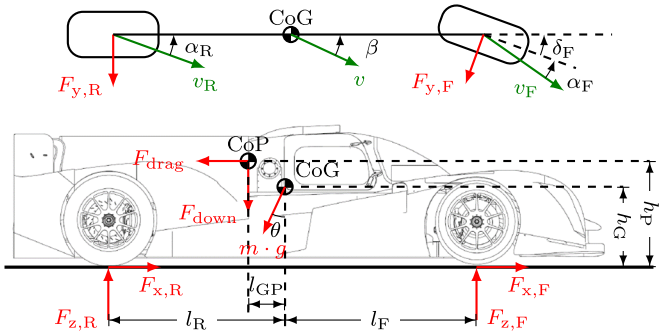

Fig. 4. Top and side view of the single-track vehicle model. The forces acting on the vehicle are shown in red and the velocity vectors are shown in green. The CoG is shown in both figures, whereas the CoP is only shown in the side view. The arrows indicate positive directions, angles, and forces.

we now separately optimize the last stint. Finally, we showcase our framework on the Zandvoort circuit for the vehicle shown in Fig. 1, with the corresponding powertrain architecture shown in Fig. 2.

C. Organization

The remainder of this article is structured as follows. Section II presents the minimum-stint-time control problem, after which Section III frames the maximum-race-distance control problem. We discuss some of the limitations of our work in Section IV and showcase our framework for a 6 h race in Section V. Finally, Section VI draws the conclusions and provides an outlook on future research.

II. Low-Level Stint Optimization

This section illustrates the minimum-stint-time control problem in the space domain since minimizing the stint time given a fixed distance represents the dual problem of maximizing distance within a fixed time. We leverage an existing convex framework [26], reformulated to a single-track model without steering and side-slip angles, as we do not consider torque-vectoring, and extend it to allow multilap optimization, whilst including the EM and battery temperature dynamics. From the time-optimal control problem, we obtain the minimum stint time for a given stint length and charge time (which is directly related to available battery energy).

Fig. 5 shows a schematic representation of the powertrain topology of the electric race car presented in Fig. 2. The EM propels both of the rear wheels through a fixed final drive (FD), while receiving energy from the battery pack via the inverter. As with most electric vehicles, the EM can also operate as a generator, thus we account for a bi-directional energy flow between the battery and the wheels. In addition, we consider auxiliary components that are powered from the main battery, such as pumps and compressors for the cooling system, as a uni-directional energy flow.

In reality, the driver controls the EM torque and the brake force through the accelerator and brake pedal, respectively, and as such we define the mechanical EM power P_m and mechanical brake power P_{brake} as the input variables. As state variables, we choose the battery energy E_b, battery temperature ϑ_b,

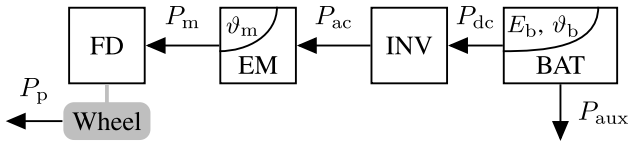

Fig. 5. Schematic layout of the electric race car powertrain topology consisting of a battery (BAT), inverter (INV), EM, and FD. The arrows indicate positive power flows of the auxiliary power P_{aux}, the electrical inverter power P_{dc}, the electrical EM input power P_{ac} and mechanical output power P_m, and the propulsion power P_p. The vehicle is rear-wheel driven, with mechanical brakes on each wheel.

EM temperature ϑ_m, and the kinetic energy of the vehicle E_{kin}. The remaining energy flows between the powertrain components are the propulsion power P_p, electrical EM power P_{ac}, electrical inverter power P_{dc}, and auxiliary supply P_{aux}. Since we formulate the control problem in the space domain, we ultimately define the model in terms of forces rather than power. Hence, we divide power by the vehicle velocity, since the space-derivative of energy is defined with respect to the vehicle.

A. Objective and Longitudinal Dynamics

In racing, the objective is to minimize the lap times over the entire race. Since we only consider a stint in the low-level control problem, the objective is to minimize the stint time t_{stint}, which is defined as

$$\min t_{stint} = \min \int_0^{S_{stint}} \frac{dt}{ds}(s)\, ds \tag{1}$$

where S_{stint} is the stint length in terms of distance and $dt/ds(s)$ is the lethargy, which is the inverse of the vehicle velocity $v(s) \geq v_{min}$, with v_{min} being a positive velocity close to standstill. To implement lethargy as a convex constraint, we define

$$\frac{dt}{ds}(s) \geq \frac{1}{v(s)} \tag{2}$$

which is a convex relaxation that holds with equality in case of an optimal solution [18].

In this study, we limit ourselves to nontorque-vectoring powertrain topologies and thereby only include the longitudinal vehicle dynamics with the use of a single-track model that captures the front and rear axle individually, as shown in Fig. 4. The single-track model was found to provide the best tradeoff between model complexity and accuracy for race strategy optimization purposes, and has been frequently applied in minimum lap time studies [10]. The longitudinal force balance is given by

$$\frac{d}{ds}E_{kin}(s) = F_{x,F}(s) + F_{x,R}(s) - F_{drag}(s) - m \cdot g \cdot \sin(\theta(s)) \tag{3}$$

where $F_{x,i}(s)$ is the longitudinal force per axle with $i \in [F, R]$ denoting the front and rear axle, respectively, $F_{drag}(s)$ is the aerodynamic drag force, m is the total mass of the vehicle, g is the gravitational constant, and $\theta(s)$ is the inclination of the track along the racing line. Hereby we assume a track with

a fixed racing line, and known altitude and banking profiles. The aerodynamic drag force is given by

$$F_{\text{drag}}(s) = \frac{c_{\text{d}} \cdot A_{\text{f}} \cdot \rho}{m} \cdot E_{\text{kin}}(s) \tag{4}$$

where c_{d} is the drag coefficient, A_{f} is the frontal area of the vehicle, and ρ is the air density. The longitudinal axle forces are defined as

$$F_{\text{x},i}(s) = F_{\text{p},i}(s) - c_{\text{r}} \cdot F_{\text{z},i}(s) - F_{\text{brake},i}(s) \tag{5}$$

where $F_{\text{p},i}(s)$ is the propulsion force per axle, c_{r} is the rolling resistance coefficient, $F_{\text{z},i}(s)$ represents the vertical axle force, and $F_{\text{brake},i}(s)$ is the force from the mechanical brakes per axle. For nondriven wheels we set $F_{\text{p},i}(s) = 0$, whereas for driven wheels we write (5) as two inequality constraints to capture the final drive losses through

$$F_{\text{x},i}(s) \leq F_{\text{m}}(s) \cdot \eta_{\text{fd}} - c_{\text{r}} \cdot F_{\text{z},i}(s) - F_{\text{brake},i}(s) \tag{6}$$

$$F_{\text{x},i}(s) \leq F_{\text{m}}(s) \cdot \frac{1}{\eta_{\text{fd}}} - c_{\text{r}} \cdot F_{\text{z},i}(s) - F_{\text{brake},i}(s) \tag{7}$$

where $F_{\text{m}}(s)$ is the mechanical output force from the EM and η_{fd} is the efficiency of the final drive, assumed constant. Due to the objective (1), in case of traction, (6) will hold with equality, whilst in the case of regenerative braking, (7) will hold with equality, thus capturing the bi-directional power flow.

The lateral force balance is defined as

$$2\ E_{\text{kin}}(s) \cdot \zeta(s) = F_{\text{y,F}}(s) + F_{\text{y,R}}(s) + m \cdot g \cdot \sin(\phi(s)) \tag{8}$$

where $\kappa(s)$ is the precomputed curvature of the optimal racing line around the track, assumed to be fixed, $F_{\text{y},i}(s)$ represents the lateral force per axle and $\phi(s)$ is the banking of the track along the racing line.

The vertical force balance consists of the static load and the aerodynamic downforce (see Fig. 4) as

$$F_{\text{z,F}}(s) + F_{\text{z,R}}(s) = m \cdot g \cdot \cos(\theta(s)) \cdot \cos(\phi(s)) + F_{\text{down}}(s) \tag{9}$$

where $F_{\text{z},i}(s)$ is the vertical force per axle and $F_{\text{down}}(s)$ is the aerodynamic downforce given by

$$F_{\text{down}}(s) = \frac{c_{\text{l}} \cdot A_{\text{f}} \cdot \rho}{m} \cdot E_{\text{kin}}(s) \tag{10}$$

where c_{l} is the lift coefficient. We consider steady-state cornering only, thereby assuming a yaw moment equilibrium given by

$$F_{\text{y,F}}(s) \cdot l_{\text{F}} = F_{\text{y,R}}(s) \cdot l_{\text{R}} \tag{11}$$

where l_i represents the horizontal distance from the respective axle to the center of gravity (CoG).

The longitudinal load transfer is determined through the pitch moment equilibrium about the orthogonal projection of the CoG on the road plane, which is defined by

$$\begin{aligned}\frac{\text{d}}{\text{d}s} E_{\text{kin}}(s) \cdot h_{\text{G}} = {} & F_{\text{z,R}}(s) \cdot l_{\text{R}} - F_{\text{z,F}}(s) \cdot l_{\text{F}} - m \\ & \cdot g \cdot \sin(\theta(s)) \cdot h_{\text{G}} \\ & - F_{\text{drag}}(s) \cdot h_{\text{P}} - F_{\text{down}}(s) \cdot l_{\text{GP}}\end{aligned} \tag{12}$$

where h_{G} is the height of the CoG with respect to the ground, h_{P} is the height of the center of pressure (CoP) with respect to the ground and l_{GP} is the horizontal distance from the CoG to the CoP.

The longitudinal and lateral forces are bounded by their respective friction circles per axle, which are defined by the convex set written as

$$\left(\frac{F_{\text{x},i}(s)}{\mu_{\text{x},i}}\right)^2 + \left(\frac{F_{\text{y},i}(s)}{\mu_{\text{y},i}}\right)^2 \leq F_{\text{z},i}(s)^2 \tag{13}$$

where $\mu_{\text{x},i}$ and $\mu_{\text{y},i}$, both assumed constant, represent the longitudinal and lateral tire friction coefficients, respectively. Although the constraint function is not convex, it specifies a convex set, which is shown in the Appendix.

The majority of racing vehicles are equipped with mechanical brakes that provide a fixed brake force ratio between the front and rear wheels. Therefore, we define a relation between the front and rear brake force as

$$F_{\text{brake,R}}(s) \cdot \delta_{\text{brake}} = F_{\text{brake,F}}(s) \cdot (1 - \delta_{\text{brake}}) \tag{14}$$

where δ_{brake} represents the brake balance with respect to the front, which is assumed to remain constant during the race. Since we are interested in finding the optimal powertrain operation, we decouple the mechanical brakes and the regenerative braking from the EM. In practice, this can be regarded as a separate driver input for regenerative braking, but the exact implementation is beyond the scope of this work.

The relation between the kinetic energy and velocity of the vehicle is defined by a convex relaxation as

$$E_{\text{kin}}(s) \geq \frac{1}{2} \cdot m \cdot v^2(s). \tag{15}$$

In contrast to single-lap scenarios, a stint is represented by the vehicle starting and stopping at the pit box with a certain number of flying laps in between. However, since we are working in the space domain, the lethargy would diverge to infinity for zero velocity. To solve this issue, we define a minimal velocity v_{min} close to a standstill and enforce this value to the initial and final velocity with

$$E_{\text{kin}}(0) = E_{\text{kin}}(S_{\text{stint}}) = \frac{1}{2} \cdot m \cdot v_{\text{min}}^2. \tag{16}$$

Finally, the vehicle should adhere to a strict speed limit, of which the exact value is track-dependent when driving through the pit lane. Therefore, we define an upper bound $v_{\text{pit,max}}$ on the vehicle velocity when the vehicle is exiting or entering the pit as

$$E_{\text{kin}}(s) \leq \frac{1}{2} \cdot m \cdot v_{\text{pit,max}}^2 \quad \forall s \in \mathcal{S}_{\text{pit}} \tag{17}$$

where $\mathcal{S}_{\text{pit}}$ is the set of distance-based positions that are part of the pit lane.

B. Electric Machine

This section derives a convex representation of the operating limits and power losses of the EM. Moreover, we derive the thermal dynamics of the EM and compare the model against real-world test data.

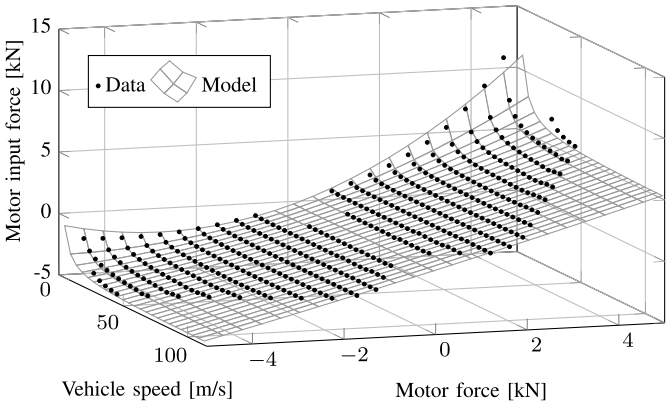

Fig. 6. Speed- and torque-dependent model of the EM. The normalized root-mean-square error (RMSE) of the model is 1.49% with respect to the maximum motor input force F_{ac}.

In general, we can distinguish between maximum torque and maximum power operating region for an EM. Translating this to constraints in the space domain results in a lower and upper bound on the mechanical output force of the EM for the maximum torque region as

$$F_{\mathrm{m}}(s) \in \left[-\frac{T_{\mathrm{m,max}} \cdot \gamma_{\mathrm{fd}}}{r_{\mathrm{w}}}, \frac{T_{\mathrm{m,max}} \cdot \gamma_{\mathrm{fd}}}{r_{\mathrm{w}}}\right] \tag{18}$$

where $T_{\mathrm{m,max}}$ is the maximum torque the EM can deliver, γ_{fd} is the final drive ratio, and r_{w} is the radius of the rear wheels. Note that we include the final drive ratio, as we define the space-derivatives with respect to the vehicle reference frame. Similarly, the mechanical output force of the EM within the maximum power region is bounded as

$$F_{\mathrm{m}}(s) \in \left[-P_{\mathrm{m,max}} \cdot \frac{\mathrm{d}t}{\mathrm{d}s}(s),\ P_{\mathrm{m,max}} \cdot \frac{\mathrm{d}t}{\mathrm{d}s}(s)\right] \tag{19}$$

where $P_{\mathrm{m,max}}$ is the maximum power the EM can deliver.

We model the EM *force* losses $F_{\mathrm{m,l}}(s)$ rather than the power losses as a function of the vehicle velocity and force of the EM. We calculate the force loss data points, denoted with $\hat{(\cdot)}$, from the EM power losses as

$$\hat{F}_{\mathrm{m,l}} = \frac{\hat{P}_{\mathrm{m,l}} \cdot \gamma_{\mathrm{fd}}}{\hat{\omega}_{\mathrm{m}} \cdot r_{\mathrm{w}}}. \tag{20}$$

In general, an EM efficiency map shows large losses at low rotational velocities. Hence, we want to include a term in our losses fit that is inversely proportional to the vehicle velocity. To ensure convexity, we model the EM losses as

$$F_{\mathrm{m,l}}(s) = x_{\mathrm{m,l}}^{\top}(s) Q_{\mathrm{m,l}} x_{\mathrm{m,l}}(s) \tag{21}$$

where $x_{\mathrm{m,l}}(s) = [(1/\sqrt{v(s)})\ (v(s))^{1/2}\ (F_{\mathrm{m}}(s)/(v(s))^{1/2})]^{\top}$ and $Q_{\mathrm{m,l}} \in \mathbb{S}_{+}^{3}$ is a symmetric positive semidefinite matrix of coefficients, whose values are determined through semidefinite programming. Fig. 6 shows the EM input force as a function of the EM output force and vehicle speed for the convex model and for the reference data. To implement the losses in a convex manner, we take the relation of the electrical EM input force $F_{\mathrm{ac}}(s)$ to the mechanical output force as

$$F_{\mathrm{ac}}(s) = F_{\mathrm{m}}(s) + F_{\mathrm{m,l}}(s) \tag{22}$$

substitute the loss model, relax it, and rewrite it to a relaxation describing a convex set as

$$(F_{\mathrm{ac}}(s) - F_{\mathrm{m}}(s)) \cdot v(s) \geq y_{\mathrm{m,l}}^{\top}(s) Q_{\mathrm{m,l}} y_{\mathrm{m,l}}(s) \tag{23}$$

where $y_{\mathrm{m,l}}(s) = [1\ v(s)\ F_{\mathrm{m}}(s)]^{\top}$. The convexity of this constraint is shown in the Appendix by writing it as a second-order conic constraint.

For the cooling circuit of the EM, we consider a conventional setup using liquid cooling and radiators, as commonly applied in motorsport. The losses are assumed to be converted to heat, thereby changing the EM temperature according to the first-order temperature ordinary differential equation (ODE) given by

$$C_{\mathrm{m}} \cdot \frac{\mathrm{d}\vartheta_{\mathrm{m}}}{\mathrm{d}t}(s) = P_{\mathrm{m,l}}(s) - P_{\mathrm{m,c}}(s) \tag{24}$$

where C_{m} is the total lumped thermal capacity of the EM, $\vartheta_{\mathrm{m}}(s)$ is the temperature of the EM (defined at the windings), $P_{\mathrm{m,l}}(s)$ are the EM power losses and $P_{\mathrm{m,c}}(s) \geq 0$ represents the power outflow to the cooling liquid as

$$P_{\mathrm{m,c}}(s) = \left(\vartheta_{\mathrm{m}}(s) - \vartheta_{\mathrm{m,c}}\right) \cdot \lambda_{\mathrm{m}} \tag{25}$$

where $\vartheta_{\mathrm{m,c}}$ represents the temperature of the cooling liquid and λ_{m} is the thermal conductivity between the EM and the cooling liquid, where we assume both parameters to be constant. In reality, the coolant temperature may change depending on the performance of the cooling system. Yet in high-level motorsports, this change in coolant temperature is relatively small compared to the change in EM temperature and therefore we deem the modeling of the underlying cooling system beyond the scope of this article. Rewriting (24) to space domain results in

$$C_{\mathrm{m}} \cdot \frac{\mathrm{d}\vartheta_{\mathrm{m}}}{\mathrm{d}s}(s) = F_{\mathrm{m,l}}(s) - F_{\mathrm{m,c}}(s) \tag{26}$$

where $F_{\mathrm{m,c}}(s) \geq 0$ is the force-equivalence of the EM cooling power. This EM cooling force is ultimately obtained by rewriting (25) to forces using a convex relaxation and linear equality constraint. To obtain a convex representation, we approximate the EM temperature as

$$\overline{\vartheta}_{\mathrm{m}}(s) = x_{\mathrm{m},\vartheta}^{\top}(s) Q_{\mathrm{m},\vartheta} x_{\mathrm{m},\vartheta}(s) + \vartheta_{\mathrm{m,0}} \tag{27}$$

where $x_{\mathrm{m},\vartheta}(s) = [1\ \vartheta_{\mathrm{m}}(s)]^{\top}$, $\vartheta_{\mathrm{m,0}}$ is an offset required to obtain positive values and $Q_{\mathrm{m},\vartheta} \in \mathbb{S}_{-}^{2}$ is a negative semidefinite matrix of coefficients, obtained through semidefinite programming. The semidefinite fit of the temperature together with the relative error is shown in Fig. 7. We select a negative semidefinite matrix since we require an upper bound on the EM temperature. Translating (25) to forces and substituting the offset of (27) results in

$$F_{\mathrm{m,c}}(s) = \left(\overline{F}_{\mathrm{m,c}}(s) + \left(\vartheta_{\mathrm{m,0}} - \vartheta_{\mathrm{m,c}}\right) \cdot \frac{\mathrm{d}t}{\mathrm{d}s}(s)\right) \cdot \lambda_{\mathrm{m}} \tag{28}$$

where $\overline{F}_{\mathrm{m,c}}(s)$ is an intermediate variable used to obtain a convex formulation through

$$\overline{F}_{\mathrm{m,c}}(s) \cdot v(s) \leq x_{\mathrm{m},\vartheta}^{\top}(s) Q_{\mathrm{m},\vartheta} x_{\mathrm{m},\vartheta}(s) \tag{29}$$

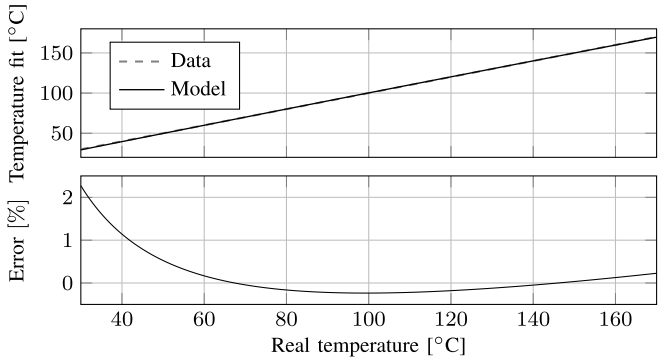

Fig. 7. Semidefinite fit of the EM temperature together with the relative error. The normalized RMSE is 0.15% with respect to the maximum temperature.

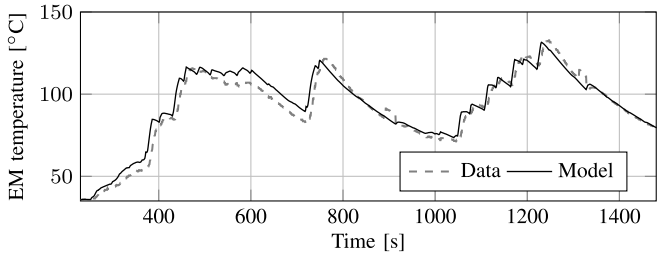

Fig. 8. Comparison between the thermal model and one of the vehicle telemetry data samples. In total, three datasets were used to fit the model parameters, of which the average normalized RMSE was 4.12% with respect to the maximum temperature of each dataset.

which can be written as a second-order conic constraint (see Appendix). Since the cooling circuit consists of liquid coolant flowing through the EM to a set of radiators, the coolant temperature cannot exceed the EM temperature, resulting in

$$F_{\mathrm{m,c}}(s) \geq 0. \tag{30}$$

To obtain the thermal parameters of the EM, we apply the convex loss- and cooling model to a combination of datasets recorded from vehicle telemetry. Fig. 8 shows a comparison between the EM temperature from one of the datasets and the thermal model.

To prevent the EM from overheating, we define an upper bound on the temperature through

$$\vartheta_{\mathrm{m}}(s) \leq \vartheta_{\mathrm{m,max}} \tag{31}$$

where $\vartheta_{\mathrm{m,max}}$ is the maximum temperature of the EM. Finally, we specify an initial value for the EM temperature as

$$\vartheta_{\mathrm{m}}(0) = \vartheta_{\mathrm{m,init}} \tag{32}$$

where $\vartheta_{\mathrm{m,init}}$ is the initial value for the temperature and is calculated during preprocessing using a lookup table that has the charge time as an input.

C. Inverter

In this section, we derive a quadratic loss model for the inverter losses. As opposed to the EM, we do not model the inverter temperature, since we assume that the motor-inverter combination is designed such that the EM is thermally limiting. We apply the general quadratic power loss model of the form

$$P_{\mathrm{dc}}(s) = \alpha_{\mathrm{inv}} \cdot P_{\mathrm{ac}}^2(s) + P_{\mathrm{ac}}(s) \tag{33}$$

where $\alpha_{\mathrm{inv}} \geq 0$ is an efficiency parameter, subject to identification. Converting this constraint to forces, rewriting and relaxing results in

$$(F_{\mathrm{dc}}(s) - F_{\mathrm{ac}}(s)) \cdot \frac{\mathrm{d}t}{\mathrm{d}s}(s) \geq \alpha_{\mathrm{inv}} \cdot F_{\mathrm{ac}}^2(s) \tag{34}$$

where $F_{\mathrm{dc}}(s)$ is the force equivalent to the electrical inverter power. The convexity of this constraint is shown in the Appendix by writing it as a second-order conic constraint.

D. Battery

This section derives a model for the battery efficiency and the power-split between the electrical inverter power and the auxiliary component power. The latter can be observed from Fig. 5 and is written as

$$P_{\mathrm{b}}(s) = P_{\mathrm{dc}}(s) + P_{\mathrm{aux}} \tag{35}$$

where $P_{\mathrm{b}}(s)$ is the battery power at the terminals. Here, the auxiliary component supply is assumed to be constant and uni-directional, while the other powers are bi-directional. Converting (35) to forces results in

$$F_{\mathrm{b}}(s) = F_{\mathrm{dc}}(s) + P_{\mathrm{aux}} \cdot \frac{\mathrm{d}t}{\mathrm{d}s}(s) \tag{36}$$

where $F_{\mathrm{b}}(s)$ is the force equivalent of the battery power at the terminals.

The battery efficiency is mostly determined by its internal resistance R_0 and open-circuit voltage V_{oc}. We derive the battery losses $P_{\mathrm{b,l}}(E_{\mathrm{b}}, \vartheta_{\mathrm{b}}, P_{\mathrm{i}})$ from a quasistatic zero-order Thévenin equivalent circuit model [27, Chapter 4.5], whereby we only consider the open-circuit voltage and internal resistance. The battery losses are given by

$$P_{\mathrm{b,l}}(E_{\mathrm{b}}, \vartheta_{\mathrm{b}}, P_{\mathrm{i}}) = \frac{1}{P_{\mathrm{sc}}(E_{\mathrm{b}}, \vartheta_{\mathrm{b}})} \cdot P_{\mathrm{i}}^2(s) \tag{37}$$

where $P_{\mathrm{sc}}(E_{\mathrm{b}}, \vartheta_{\mathrm{b}}) = (V_{\mathrm{oc}}^2(E_{\mathrm{b}})/R_0(E_{\mathrm{b}}, \vartheta_{\mathrm{b}}))$ is the short-circuit power [28]. In reality, both the internal resistance and open-circuit voltage are a function of the battery temperature and energy. Since the battery reaches its thermal limit at the end of the charging process and has to be cooled during driving, it is operated at a relatively large temperature window. Therefore, the heat generation of the battery due to losses can vary significantly during driving. However, since the influence of the battery temperature on the open-circuit voltage is rather small (less than 0.25% according to manufacturer datasheets) within the operating window in racing scenarios, we neglect the dependency of the open-circuit voltage on temperature [29], [30]. To capture the impact of temperature on the internal resistance, we apply a correction factor inversely proportional to the battery temperature temperature [31], [32] to obtain

$$P_{\mathrm{sc}}(E_{\mathrm{b}}, \vartheta_{\mathrm{b}}) = \frac{V_{\mathrm{oc}}^2(E_{\mathrm{b}})}{R_0(E_{\mathrm{b}})} \cdot \frac{\vartheta_{\mathrm{b}}(s)}{\vartheta_{\mathrm{ref}}} \tag{38}$$

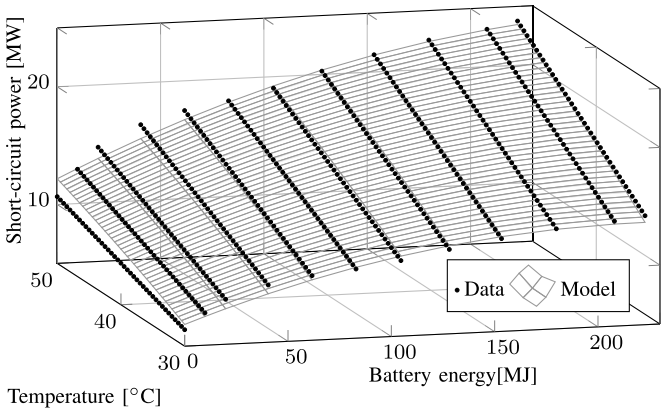

Fig. 9. Temperature- and energy-dependent battery model compared to the calculated short-circuit power using manufacturer datasheets. The normalized RMSE of the model is 2.23% with respect to the maximum short-circuit power.

where ϑ_{ref} represents the reference temperature at which the battery data are measured. Similar to the thermal EM model, we fit the short-circuit power in a convex manner through

$$P_{\text{sc}}(s) = x_{\text{b,1}}^{\top}(s) Q_{\text{b,1}} x_{\text{b,1}}(s) + P_{\text{sc,0}} \tag{39}$$

where $x_{\text{b,1}}(s) = [1 \ E_{\text{b}}(s) \ \vartheta_{\text{b}}(s)]^{\top}$, $P_{\text{sc,0}}$ is an offset required to obtain positive values and $Q_{\text{b,1}} \in \mathbb{S}_{-}^{2}$ is a negative semidefinite matrix of coefficients, identified through semidefinite programming. Again, we select a negative semidefinite matrix, since it is optimal to maximize the short-circuit force, and thereby require an upper bound. The temperature- and energy-dependent model of the short-circuit power is shown in Fig. 9. Translating (38) to forces and substituting the offset of (39) results in

$$F_{\text{sc}}(s) = \overline{F}_{\text{sc}}(s) + P_{\text{sc,0}} \cdot \frac{\mathrm{d}t}{\mathrm{d}s}(s) \tag{40}$$

where $F_{\text{sc}}(s)$ is the short-circuit force and $\overline{F}_{\text{sc}}(s)$ is an intermediate variable used to obtain a convex formulation through

$$\overline{F}_{\text{sc}}(s) \cdot v(s) \leq x_{\text{b,1}}^{\top}(s) Q_{\text{b,1}} x_{\text{b,1}}(s). \tag{41}$$

To obtain the battery losses during discharging $F_{\text{b,l}}(s)$, we translate (37) to forces and relax it, which results in

$$F_{\text{b,l}}(s) \cdot F_{\text{sc}}(s) \geq F_{\text{i}}^{2}(s) \tag{42}$$

where $F_{\text{i}}(s)$ is the internal battery force, which ultimately dictates a change in battery energy. To prevent the battery losses and short-circuit force from cooling the battery, we explicitly define

$$F_{\text{b,l}}(s) \geq 0 \tag{43}$$

$$F_{\text{sc}}(s) \geq 0. \tag{44}$$

In general, the heat generation of a Li-ion battery is different between charging and discharging conditions. As the direction of power flow frequently changes during a lap, it is important to capture the additional heat generation during negative power flow. To capture this behavior, we add an additional term to the battery losses to represent distinct heat generation during charging, compared to discharging. This means that we effectively have a different battery efficiency during charging and discharging [27]. Since this term should only be present during negative power flow, we implement a set of inequality constraints similar to the final drive losses as

$$F_{\text{i}}(s) \geq F_{\text{b}}(s) + F_{\text{b,l}}(s) \tag{45}$$

$$F_{\text{i}}(s) \geq (1 - \alpha_{\text{ch}}) \cdot F_{\text{b}}(s) + F_{\text{b,l}}(s) \tag{46}$$

where $F_{\text{b}}(s)$ is the battery force at the terminals and α_{ch} is a coefficient that represents the distinct charging losses. Note that $\alpha_{\text{ch}} \geq 0$ results in higher losses during charging, compared to discharging, whereas $\alpha_{\text{ch}} \leq 0$ results in higher losses during discharging, compared to charging. In energy-limited scenarios, (45) will hold with equality during discharging, whereas (46) will hold with equality during charging.

In contrast to the EM cooling, where the difference between the EM temperature and the ambient temperature (in the order of 100 °C) is sufficient to apply radiators, the difference between the battery temperature and the ambient air is significantly lower (in the order of 25 °C). Therefore, it is common to apply a refrigerant circuit instead of radiators to cool the battery during fast-charging pit stops and driving, which allows the coolant temperature to drop below ambient level. Again, all losses are assumed to be converted to heat, thereby changing the battery temperature according to the first-order temperature ODE given by

$$C_{\text{b}} \cdot \frac{\mathrm{d}\vartheta_{\text{b}}}{\mathrm{d}t}(s) = P_{\text{b,l}}(s) - P_{\text{b,c}}(s) \tag{47}$$

where C_{b} is the total lumped thermal capacity of the battery, $\vartheta_{\text{b}}(s)$ is the temperature of the battery and $P_{\text{b,c}}(s) \geq 0$ represents the power outflow from the battery cells to the cooling liquid. Since we consider a battery cooling circuit where the coolant temperature can be actively controlled, the cooling power is free within the bounds defined as

$$0 \leq P_{\text{b,c}}(s) \leq \left(\vartheta_{\text{b}}(s) - \vartheta_{\text{b,c}}\right) \cdot \lambda_{\text{b}} \tag{48}$$

where $\vartheta_{\text{b,c}}$ represents the lowest achievable temperature of the cooling liquid and λ_{b} is the thermal conductivity between the battery cells and the cooling liquid, where again we assume both parameters to be constant. Rewriting (47) to space domain results in

$$C_{\text{b}} \cdot \frac{\mathrm{d}\vartheta_{\text{b}}}{\mathrm{d}s}(s) = F_{\text{i}}(s) - F_{\text{b}}(s) - F_{\text{b,c}}(s) \tag{49}$$

where $F_{\text{b,c}}(s) \geq 0$ is the force-equivalence of the battery cooling power. Note that we explicitly use the difference between the internal battery force and the battery force at the terminals to include the additional charging losses. Similarly as with the EM cooling, we approximate the battery temperature as

$$\overline{\vartheta}_{\text{b}}(s) = x_{\text{b},\vartheta}^{\top}(s) Q_{\text{b},\vartheta} x_{\text{b},\vartheta}(s) + \vartheta_{\text{b,0}} \tag{50}$$

where $x_{\text{b},\vartheta}(s) = [1 \ \vartheta_{\text{b}}(s)]^{\top}$, $\vartheta_{\text{b,0}}$ is an offset required to obtain positive values and $Q_{\text{b},\vartheta} \in \mathbb{S}_{-}^{2}$ is a negative semidefinite matrix of coefficients, obtained through semidefinite programming. The semidefinite fit of the battery temperature is similar to Fig. 7, except that the normalized RMSE is reduced to 0.034%

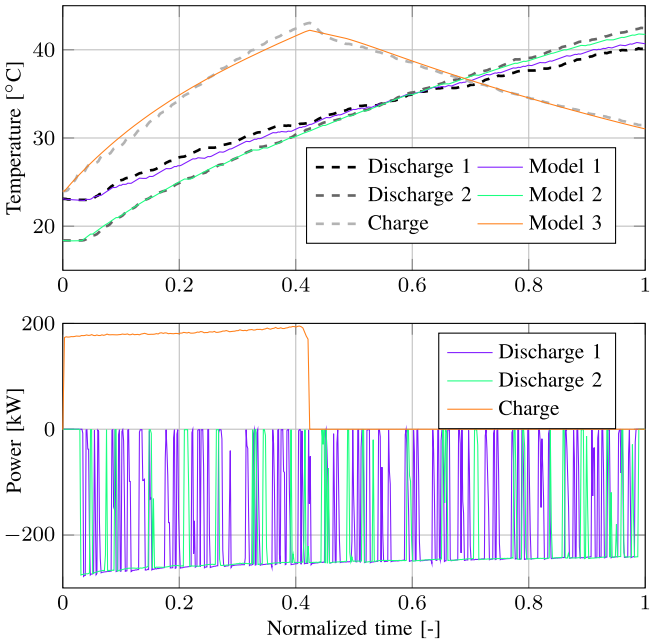

Fig. 10. Comparison between the thermal model and three datasets, of which two represent a dynamic discharge (violet and green) and one represents a constant current charge profile followed by a cooldown period (orange). The average normalized RMSE is 0.87% with respect to the maximum temperature of each dataset. Both the modeled and the measured temperatures were obtained with the corresponding battery power profiles shown in the lower plot.

due to the smaller temperature window. Translating (48) to forces and substituting the offset of (50) results in

$$F_{\mathrm{b,c}}(s) = \left(\overline{F}_{\mathrm{b,c}}(s) + \left(\vartheta_{\mathrm{b,0}} - \vartheta_{\mathrm{b,c}}\right) \cdot \frac{\mathrm{d}t}{\mathrm{d}s}(s)\right) \cdot \lambda_{\mathrm{b}} \tag{51}$$

where $\overline{F}_{\mathrm{b,c}}(s)$ is an intermediate variable used to obtain a convex formulation (see Appendix) through

$$\overline{F}_{\mathrm{b,c}}(s) \cdot v(s) \leq x_{\mathrm{b},\vartheta}^{\top}(s) Q_{\mathrm{b},\vartheta} x_{\mathrm{b},\vartheta}(s). \tag{52}$$

As the coolant temperature cannot exceed the battery temperature, we define

$$F_{\mathrm{b,c}}(s) \geq 0. \tag{53}$$

To obtain the thermal parameters of the battery, we apply the convex loss and cooling model to a combination of datasets recorded from vehicle telemetry. Fig. 10 shows a comparison between the battery temperature from various datasets and the thermal model, demonstrating that our model can accurately capture dynamic discharging as well as charging profiles.

To ensure safe operation of the battery, we define an upper bound on the temperature through

$$\vartheta_{\mathrm{b}}(s) \leq \vartheta_{\mathrm{b,max}} \tag{54}$$

where $\vartheta_{\mathrm{b,max}}$ is the maximum temperature of the battery. Due to the relatively long charge time, compared to the refueling time of a conventional race car, it is essential to minimize the charge time. Therefore, we assume that the battery temperature reaches the upper limit at the end of charging since the temperature is the main limitation. Hence, we enforce the initial battery temperature to be at the upper bound through

$$\vartheta_{\mathrm{b}}(0) = \vartheta_{\mathrm{b,max}}. \tag{55}$$

Finally, we specify a terminal value for the battery temperature as

$$\vartheta_{\mathrm{b}}(S_{\mathrm{stint}}) \leq \vartheta_{\mathrm{b,N}} \tag{56}$$

where $\vartheta_{\mathrm{b,N}}$ is the terminal value for the temperature and is calculated during preprocessing using a lookup table having the charge time as an input.

The energy consumption of the battery is modeled as

$$\frac{\mathrm{d}}{\mathrm{d}s} E_{\mathrm{b}}(s) = -F_{\mathrm{i}}(s) \tag{57}$$

and we constrain the battery energy as

$$E_{\mathrm{b,min}} \leq E_{\mathrm{b}}(s) \leq E_{\mathrm{b,max}} \tag{58}$$

where $E_{\mathrm{b,min}}$ and $E_{\mathrm{b,max}}$ correspond to the battery energy at the lower and upper state of energy (SoE) bound, respectively. Since the voltage of the battery increases with the battery energy, it is optimal to operate the battery at higher energy levels. Therefore, we set the initial battery energy to the upper bound and constrain the terminal battery energy according to the amount of energy charged after driving as

$$E_{\mathrm{b}}(0) = E_{\mathrm{b,0}} \tag{59}$$

$$E_{\mathrm{b}}(S_{\mathrm{stint}}) \geq E_{\mathrm{b,0}} - E_{\mathrm{b,ch}} \tag{60}$$

where $E_{\mathrm{b,0}}$ is the initial battery energy and $E_{\mathrm{b,ch}}$ is the energy the battery receives during charging. In this way, the battery is guaranteed to be charged back to the upper energy bound in energy-limited scenarios. To calculate the battery energy during charging, we leverage a lookup table with input charge time t_{charge} and output $E_{\mathrm{b,ch}}$ for a given charging current profile during preprocessing.

E. Low-Level Optimization Problem

This section presents the minimum-stint-time control problem of the electric race car. Given a predefined stint length and charge time, we formulate the control problem using the state variables $x = (E_{\mathrm{kin}}, E_{\mathrm{b}}, \vartheta_{\mathrm{b}}, \vartheta_{\mathrm{m}})$ and the control variables $u = (F_{\mathrm{m}}, F_{\mathrm{brake,F}}, F_{\mathrm{brake,R}})$ as follows.

Problem 1 (Minimum-Stint-Time Control Strategy): The minimum-stint-time control strategies are the solution of

$$\begin{aligned} \min \quad & \int_0^{S_{\mathrm{stint}}} \frac{\mathrm{d}t}{\mathrm{d}s}(s)\,\mathrm{d}s \\ \text{s.t.} \quad & (2) - (19), (23), (26), (28) - (32), (34) \\ & (36), (40) - (46), (49), (51) - (60). \end{aligned}$$

Since the feasible domain and the cost function are convex, the low-level control problem is fully convex, and therefore we can compute a globally optimal solution with standard nonlinear programming methods.

III. High-Level Race Optimization

In this section, we present the high-level maximum-race-distance control problem. First, we formulate the maximum-race-distance control problem that optimizes the stint length and charge time for a predefined number of pit stops. Second, we model the minimum stint time by leveraging the low-level control problem and optimizing for various combinations of stint length and initial battery energy, as was shown in Fig. 3. Finally, we extend the maximum-race-distance control problem to allow joint optimization of the stint length, charge time, and number of pit stops.

A. Mixed-Integer Control Problem

We define the high-level control problem for a predefined number of pit stops in *stint domain* so that we have a fixed and finite optimization horizon. Here, each index in the optimization variables represents a stint. The goal is then to maximize the driven distance as the sum of all completed laps during the stints as

$$\max S_{\text{race}} = \max \sum_{k=0}^{n_{\text{stops}}} S_{\text{lap}} \cdot N_{\text{laps}}(k) \tag{61}$$

where S_{race} is the total race distance, n_{stops} is the predefined number of pit stops, $N_{\text{laps}}(k) \in \mathbb{N},\ \forall\, k \in [0, \ldots,\ n_{\text{stops}} - 1]$ is the stint length and $\mathbb{N}$ the set of natural numbers, and S_{lap} is the length of one lap. Since the vehicle starts and stops at the pit box, the stint length should be an integer number of laps. As it is unlikely that the vehicle is exactly at the finish line when the race time limit is reached, we allow the final stint length to be a noninteger number of laps. This way, we have $n_{\text{stops}} + 1$ stints for n_{stops} pit stops, and thus we have n_{stops} integer stint lengths and one final noninteger stint length.

The race can be divided into the car driving a stint and the car recharging the battery during pit-stops. The total elapsed time $t_{\text{tot}}(k)$ is then updated after every pit stop by adding both the time to complete the stint $t_{\text{stint}}(k) \geq 0$ and the time spent on charging $t_{\text{charge}}(k) \geq 0$ according to

$$t_{\text{tot}}(k+1) = t_{\text{tot}}(k) + t_{\text{stint}}(k) + t_{\text{charge}}(k) \quad \forall k \in \left[0, n_{\text{stops}} - 1\right]. \tag{62}$$

Since we do not have a pit stop after the final stint, the elapsed time after the final stint is defined as

$$t_{\text{tot}}\left(n_{\text{stops}} + 1\right) = t_{\text{tot}}\left(n_{\text{stops}}\right) + t_{\text{stint}}\left(n_{\text{stops}}\right). \tag{63}$$

Moreover, we define the elapsed time counter to start at the beginning of the race, and the elapsed time after the final stint should not exceed the total race time limit t_{race}, resulting in

$$t_{\text{tot}}(0) = 0 \tag{64}$$

$$t_{\text{tot}}\left(n_{\text{stops}} + 1\right) \leq t_{\text{race}}. \tag{65}$$

We then decompose the total race into blocks consisting of the vehicle first driving a stint followed by a pit stop in which the battery is charged. Assuming that a stint is always energy-limited, the charge time uniquely defines the terminal battery energy for the prior stint and is not influenced by other stints. Furthermore, we assume that the battery is thermally limited during charging, which allows us to precalculate the maximum terminal battery temperature for the prior stint through backward integration of the battery temperature dynamics during charging. Thereby, we uniquely base the terminal battery temperature on the charge time, without being influenced by other stints. Finally, we assume that the EM temperature reaches the upper limit at the end of driving and assume that the charge times across consecutive stints remain constant. This allows us to calculate the EM temperature at the beginning of the stint by integrating the EM temperature dynamics during charging. This way, we uniquely define the initial EM temperature on the charge time.

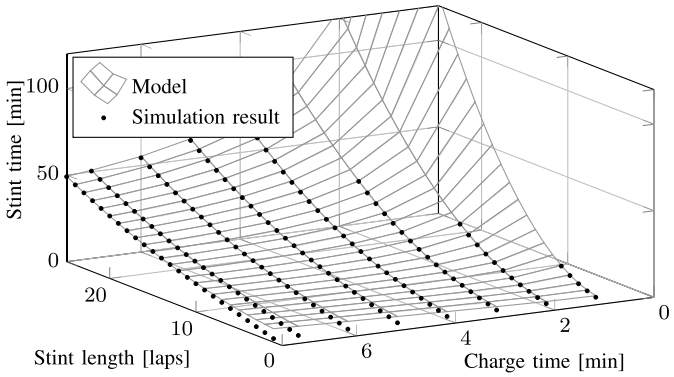

Fig. 11. Fit of optimization results for a combination of stint lengths and charge times. The normalized RMSE of the fit is 2.2% with respect to the maximum stint time.

To ensure that the battery is not overcharged, we apply an upper bound on the charge time through

$$t_{\text{charge}}(k) \leq t_{\text{charge,max}} \tag{66}$$

where $t_{\text{charge,max}}$ is the maximum charge time corresponding to charging the battery from the lower to the upper energy level. Finally, the time to complete the stint is obtained by solving the low-level control problem, which we explain in Section III-B.

B. Stint Time Model

In this section, we derive a method for modeling the stint time as a function of the stint length and charge time during the pit stop prior to the stint. We solve the low-level control Problem 1 for a combination of stint lengths and charge times to obtain the respective achievable minimum stint time. In such a manner, we can create the lookup table with stint time as a function of stint length and charge time shown in Fig. 11. Thereby, the charge time and terminal battery energy are linked through a predefined charging profile, see Section II-D, whereas the terminal battery temperature and initial EM temperature are calculated during preprocessing based on the charge time solely, see Section II-B and II-D. As the stint time increases for larger stint lengths and shorter charge times, similar to the EM loss fit in Section II-B above, we approximate the low-level optimization results via the continuous function

$$t_{\text{stint}}(k) = x_{\text{s}}^{\top}(k)\, Q_{\text{s}}\, x_{\text{s}}(k) \tag{67}$$

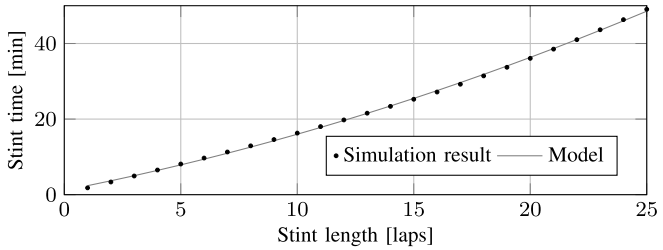

Fig. 12. Fit of the final stint times for a range of stint lengths. The normalized RMSE of the fit is 0.60% with respect to the maximum stint time.

where $x_{\mathrm{s}}(k) = [(1/(t_{\mathrm{charge}}(k))^{1/2}) \quad (t_{\mathrm{charge}}(k))^{1/2} \quad (N_{\mathrm{laps}}(k)/(t_{\mathrm{charge}}(k))^{1/2})]^\top$ and $Q_{\mathrm{s}} \in \mathbb{S}^3_+$ is a symmetric positive semidefinite matrix of coefficients. The result of the fit is shown in Fig. 11. For a convex implementation, we relax and rewrite (67) to

$$t_{\mathrm{stint}}(k) \cdot t_{\mathrm{charge}}(k) \geq y_{\mathrm{s}}(k)^\top Q_{\mathrm{s}} y_{\mathrm{s}}(k) \tag{68}$$

where $y_{\mathrm{s}}(k) = [1 \quad t_{\mathrm{charge}}(k) \quad N_{\mathrm{laps}}(k)]^\top$, and convert this relaxation to a conic constraint [33] as

$$t_{\mathrm{stint}}(k) + t_{\mathrm{charge}}(k) \geq \left\| \begin{matrix} 2 \cdot z_{\mathrm{s}}(k) \\ t_{\mathrm{stint}}(k) - t_{\mathrm{charge}}(k) \end{matrix} \right\|_2 \tag{69}$$

where $z_{\mathrm{s}} = L_{\mathrm{s}} y_{\mathrm{s}}(k)$ with L_{s} being the Cholesky factorization of Q_{s} [33]. Since it is optimal to minimize stint time, this constraint will hold with equality at the optimum.

The final stint of the race is not followed by a pit stop in which the battery is charged, which means that the battery can be fully depleted and there is no margin needed in the battery temperature. Therefore, we separately model the final stint by solving the low-level control Problem 1 for a range of stint lengths, with a fixed charge time $t_{\mathrm{charge}}(n_{\mathrm{stops}}) = t_{\mathrm{charge,max}}$ and terminal battery temperature $\vartheta_{\mathrm{b,N}} = \vartheta_{\mathrm{b,max}}$. With the charge time being fixed, we can then model the final stint time by a quadratic function with the stint length as

$$t_{\mathrm{stint}}\left(n_{\mathrm{stops}}\right) \geq D_{\mathrm{s,f}}^\top x_{\mathrm{s,f}} \tag{70}$$

where $D_{\mathrm{s,f}}$ is a vector of coefficients and $x_{\mathrm{s,f}} = [N_{\mathrm{laps}}^2(n_{\mathrm{stops}}) \quad N_{\mathrm{laps}}(n_{\mathrm{stops}}) \quad 1]^\top$. Fig. 12 shows the quadratic fit of the final stint time model.

C. Optimal Pit Stop Strategy

In Sections III-A and III-B, we introduced the objective and constraints for the high-level control problem when optimizing the race strategy for a predefined number of pit stops. In this section, we apply some modifications in order to jointly optimize the stint lengths, charge times, and number of pit stops, thereby removing the need to search over a large space of predefined number of pit stops.

We define a binary variable $b_{\mathrm{pit}}(k)$ that indicates whether pit stop and stint k is taken or skipped as

$$b_{\mathrm{pit}}(k) = \begin{cases} 0, & \text{if stint and stop skipped} \\ 1, & \text{if stint and stop taken} \end{cases} \tag{71}$$

and include it in (67) via the big-M formulation [34]

$$t_{\mathrm{stint}}(k) \geq x_{\mathrm{s}}(k)^\top Q_{\mathrm{s}} x_{\mathrm{s}}(k) - M \cdot \left(1 - b_{\mathrm{pit}}(k)\right) \tag{72}$$

where $M \gg t_{\mathrm{stint,max}}$. This way, we obtain the original constraint if $b_{\mathrm{pit}}(k) = 1$ and we obtain a negative lower bound when $b_{\mathrm{pit}}(k) = 0$. By defining

$$t_{\mathrm{stint}}(k) \geq 0 \tag{73}$$

$$t_{\mathrm{charge}}(k) \geq 0 \tag{74}$$

the kth stint time and charge time will be pushed to zero, hence skipping the stint. We convert (72) to a cone as

$$\begin{aligned} &M \cdot \left(1 - b_{\mathrm{pit}}(k)\right) + t_{\mathrm{stint}}(k) + t_{\mathrm{charge}}(k) \\ &\quad \geq \left\| \begin{matrix} 2 \cdot z_{\mathrm{s}}(k) \\ M \cdot \left(1 - b_{\mathrm{pit}}(k)\right) + t_{\mathrm{stint}}(k) - t_{\mathrm{charge}}(k) \end{matrix} \right\|_2. \end{aligned} \tag{75}$$

Hence, whenever a stint is skipped, the corresponding stint time and charge time will be zero if an optimal solution is obtained. To prevent the stint length from diverging to infinity whenever the stint is actually skipped, i.e., $b_{\mathrm{pit}}(k) = 0$, we define an upper bound on stint length as

$$N_{\mathrm{laps}}(k) \leq N_{\mathrm{laps,max}} \cdot b_{\mathrm{pit}}(k) \tag{76}$$

where $N_{\mathrm{laps,max}}$ is the maximum stint length that was used to obtain the lookup table. This will ensure $N_{\mathrm{laps}}(k) = 0$ whenever $b_{\mathrm{pit}}(k) = 0$. Since the final stint is not constrained by a lower terminal battery temperature and can deplete the battery without spending time on charging afterward, the final stint has to be part of the optimal race strategy. We ensure this by writing

$$b_{\mathrm{pit}}(k+1) \geq b_{\mathrm{pit}}(k) \quad \forall k \in \left[0, n_{\mathrm{stops}} - 1\right]. \tag{77}$$

Suppose we set the length of the variables to N and that x stints and stops are skipped. Then, the first x entries in b_{pit} will be zero and the last $N - x$ entries will be one. In this way, the final stint is always taken and the search space for the solver is reduced.

D. High-Level Optimization Problem

This section presents the maximum-race-distance control problem of the electric race car. Given a predefined race time, we formulate the control problem using the state variables $x = (t_{\mathrm{tot}})$ and the control variables $u = (t_{\mathrm{charge}}, N_{\mathrm{laps}}, b_{\mathrm{pit}})$ as follows.

Problem 2 (Maximum-Race-Distance Strategies): The maximum-race-distance strategies are the solution of

$$\begin{aligned} &\max \sum_{k=0}^{n_{\mathrm{stops}}} S_{\mathrm{lap}} \cdot N_{\mathrm{laps}}(k) \\ &\text{s.t. (62)} - \text{(66)}, \text{(70)}, \text{(73)} - \text{(77)}. \end{aligned}$$

Since Problem 2 can be solved with mixed-integer second-order conic programming solvers, we can guarantee global optimality upon convergence [35], [36].

IV. Discussion

A few comments are in order. First, we assume that endurance racing tires do not degrade significantly within a single stint, considering that the vehicle is operated less at the grip limits and the stints are relatively short, compared to

conventional endurance race cars. The tires can be changed every stint without additional time loss in the pit lane since the charging time is much longer than the tire change time. Furthermore, we assume that the tires are operated at their average operating temperature. Therefore, we disregard the influence of tire wear and tire temperature on the available grip level. Yet the high-level control problem can be readily extended to capture these dynamics if the lookup table is devised accounting for tire degradation. Second, we assume that the time gained from starting the race from the grid compared to the pit lane is negligible in a full endurance race. Hence, we do not separately optimize the first stint. Third, when the battery temperature is not an active constraint, the battery cooling relaxes in order to maximize the battery efficiency. Yet this can be interpreted as the battery coolant temperature is controlled by the refrigerant cooling system, which allows reduced cooling power, assuming that the system can cope with the requested coolant temperature changes. Fourth, in scenarios where the battery or EM temperature is very limiting and the lower battery energy limit is not reached, it may occur that (2) relaxes due to the positive contribution of a higher lethargy in (28), (40), and (51). In these cases, the solution will not reflect reality anymore and it should be disregarded. Yet from a high-level perspective, these solutions cannot be part of the optimal race strategy, since charging the battery more than needed is suboptimal. In fact, these situations were not found to be part of the optimal strategies in this study, as shown in Section V below. If a stint with a relaxed lethargy is not part of the optimal race strategy, it is guaranteed that the physically correct solution of the same stint will not be part of the optimal strategy either, since it is always worse or equal, compared to the convex solution. Fifth, we assume a fixed value for the terminal EM temperature when precalculating the bound on the initial EM temperature. However, it can occur that this value is not reached, e.g., in scenarios where the EM temperature is not an active constraint. In these situations, the temperature trajectories might not reflect reality, yet this does not affect the resulting solution, as there are no other states that depend on the EM temperature. Finally, we disregarded dynamic events, such as competitor interaction. Therefore, the results represent the theoretical optimal race strategy, which can be regarded as an upper bound on what is achievable in practice. The methods could be modified and applied online to account for such events, but this is beyond the current scope.

V. Results

This section presents numerical results for both the low- and high-level control problems. We base our use case on the driven electric endurance race car of InMotion [1], shown in Fig. 1, performing an 11-lap stint at the Zandvoort circuit for the low-level control problem and a 6 h race at the same circuit for the high-level control problem. First, we discuss the numerical solutions for both control problems. Second, we validate the high-level control problem by comparing the optimal race strategy against fixed-pit-stop-number strategies and compare the results to the expected optimal combinations of stint length and charge time. Although the model is capable of capturing the inclination and banking of the track, the results were generated for a flat track, since there is no open-access data of the Zandvoort circuit.

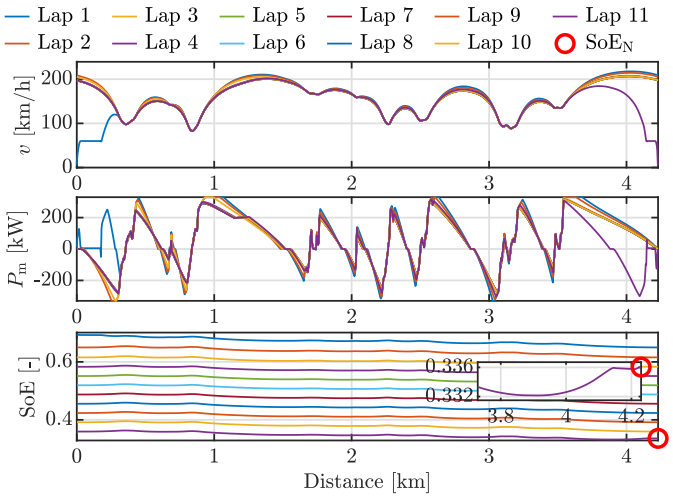

Fig. 13. Velocity, EM power, and battery SoE trajectories per lap for an 11-lap stint. The battery energy is an active constraint, thus the stint is energy-limited. The EM power shows a gradual decrease at high velocities, thus indicating energy management. The zoomed-in view window corresponds to the final 500 m of the stint.

For the discretization of the model, we apply the trapezoidal method with a fixed step size of $\Delta s = 4$ m. We parse the low-level control problem with CasADi [37] and solve it using IPOPT [38] combined with the MA57 linear solver [39], whilst we parse the high-level control problem with YALMIP [40] and solve it using MOSEK [41]. We perform the numerical optimization on an Intel Core i7-4710MQ 2.5 GHz processor and 8 GB of RAM. Thereby, the computation time for solving the low-level problem was about 0.68 s of parsing and 61 s of solving, whereas the high-level problem needed 0.21 s of parsing and 4.5 s of solving.

A. Low-Level Optimization

In this section, we compute the optimal trajectories for a stint of 11 laps around the Zandvoort circuit. We set the terminal battery capacity to the energy level corresponding to a 5 min charge time using constant current charging, which means that the battery is partially charged. The total stint time is about 1126 s with an average flying lap time of 101 s (not counting the first and last lap).

The velocity profile together with the EM power and SoE per lap is shown in Fig. 13. Furthermore, the total stint velocity profile together with the powertrain losses, SoE, battery temperature, and EM temperature is shown in Fig. 14.

First, we observe that the velocity profiles of the first four consecutive laps are slightly different, which is due to the EM temperature being an active constraint. Since the EM temperature starts below the limit, the velocity in the first laps is the highest and decreases as the EM temperature reaches the upper limit. In this scenario, the terminal battery temperature is not an active constraint, since the battery temperature is kept at the maximum level during the first half of the stint by reducing the cooling power, thereby increasing the battery

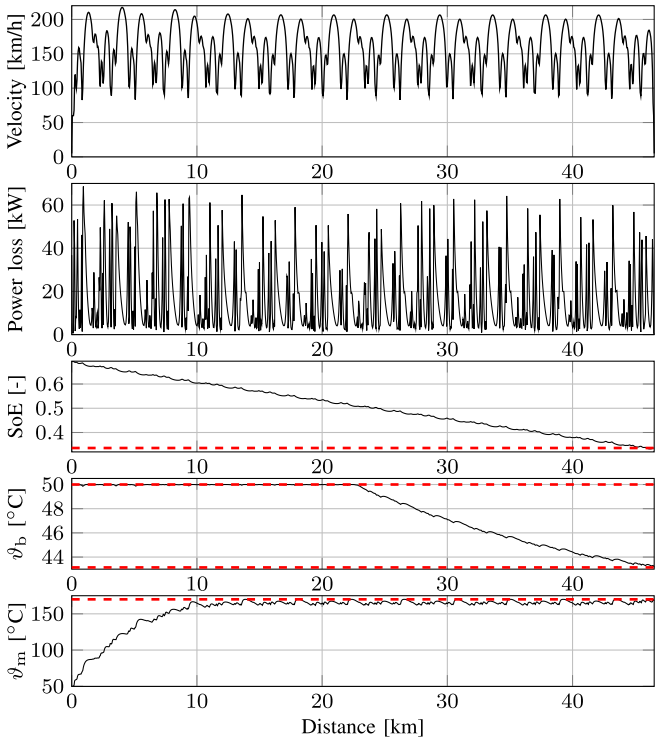

Fig. 14. Velocity, powertrain losses, battery SoE, battery temperature, and EM temperature trajectories for an 11-lap stint. The battery energy is an active constraint, thus the stint is energy-limited and energy management is needed. Furthermore, the maximum EM temperature is reached multiple times throughout the stint. Therefore, the velocity profile decreases when the maximum EM temperature is reached.

efficiency. In the second half of the stint, the battery temperature decreases gradually by applying maximum cooling to reach the required terminal value. If the terminal battery temperature were an active constraint, we would observe a gradual decrease in temperature over the entire stint, as shown in the Appendix for illustration purposes. Second, the EM power decreases gradually before the vehicle reaches a corner and regenerative braking is applied. However, both the power during traction as well as the regenerative braking power decrease when the EM temperature limit is reached. In general, the velocity profile shows smooth behavior (i.e., the acceleration of the vehicle is within a relatively small value range), which is typical for energy-limited scenarios [12], [14], [15], since regenerative braking is used instead of the mechanical brakes to reduce the velocity before cornering. Third, we observe that the battery energy exceeds the terminal value before the end of the stint. Since the battery is partially charged in this scenario, the absolute lower energy limit is not reached. With the use of regenerative braking, the battery energy then reaches the terminal value exactly at the end of the stint, indicating an energy-limited scenario. Finally, Fig. 15 shows the normalized lateral and longitudinal forces per axle, along with the maximum grip limit defined by the friction coefficient. Since the vehicle in this study is rear-wheel driven ($F_{\mathrm{p,F}} = 0$), the front axle only provides negative forces in the longitudinal direction. It can be noticed that the data points do not show the typical diamond-like pattern for the front axle forces that is expected in racing scenarios [42]. This

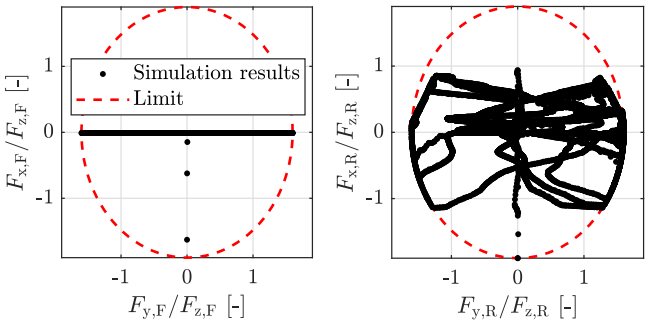

Fig. 15. Friction circles per axle showing the normalized longitudinal and lateral forces. The vehicle is rear-wheel driven and braking is done mostly using the EM. Therefore, the front axle (left) mostly generates lateral forces, whereas the rear axle (right) shows more combined forces.

is because the mechanical brakes are only used during pit entry at the end of the stint and because the vehicle applies regenerative braking to slow down for cornering. Moreover, both the front and rear axles are operated at the lateral grip limit in corners, indicating that the acceleration throughout the corners is maximized.

B. High-Level Optimization

This section presents the optimal race strategy in terms of the number of pit stops, stint length, and charge time, and we compare it against the strategies optimized for a fixed number of pit stops. We select a 6 h race, yet longer races can be solved as well with our approach, considering the very low computational times needed by our high-level framework to converge. To link the terminal battery energy $E_{\mathrm{b}}(S_{\mathrm{stint}})$ to the charge time t_{charge}, we apply constant current charging, which is in line with the implementation on the actual vehicle. Furthermore, we calculate the terminal battery temperature $\vartheta_{\mathrm{b,N}}$ using the losses that correspond to the constant current profile and obtain the initial EM temperature $\vartheta_{\mathrm{m,init}}$ by applying maximum cooling power, for the given charge time.

Fig. 16 shows the evolution of the completed laps as a function of time for various fixed pit stop strategies. We observe that the optimal strategy of 14 stops results in the largest amount of completed laps, thereby confirming that it is indeed optimal in terms of number of pit stops. The difference in covered race length between the optimal and fixed-pit-stop-number strategies can exceed multiple laps and hence significantly affect the final race outcome in terms of finishing position, highlighting the importance of jointly optimizing the number of pit stops. Furthermore, we compare the optimal race strategy against a strategy that repeats the global optimal stint of 11 laps and 4.7 min charging, until the race ends. Although the stints used in this strategy are globally optimal from a stint perspective, it does not cover the largest distance within the 6 h time window, which makes the strategy suboptimal from a race perspective. This is because a pure repetition of the optimal stint does not perfectly fit within the 6 h race. Instead, it is beneficial to slightly deviate from the optimal stint, so that the stints fit better within the race, as done by the optimal race strategy. This shows that the optimal race strategy is not necessarily the same as the

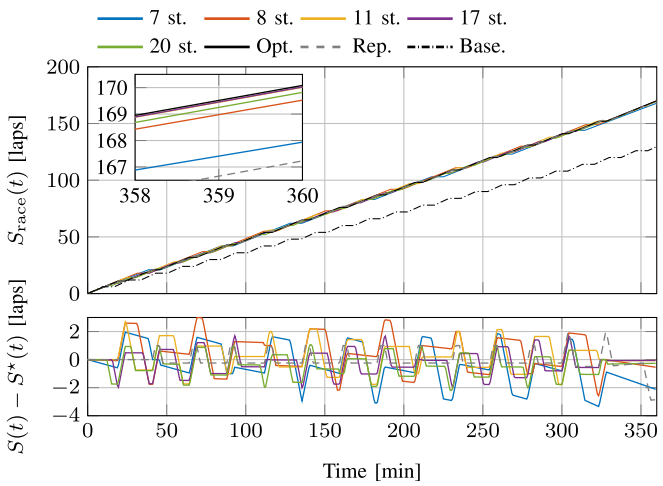

Fig. 16. Evolution of the completed laps as a function of time for the optimal strategy (black) and the strategies optimized for a fixed number of pit stops. The dashed data show a repetition strategy of the global optimal stint and the dash-dotted data show a baseline strategy. The zoomed-in view window corresponds to the final 2 min of the race and illustrates the difference in race distance between the optimized strategies, showing that jointly optimizing the number of stints can significantly outperform other strategies by multiple laps.

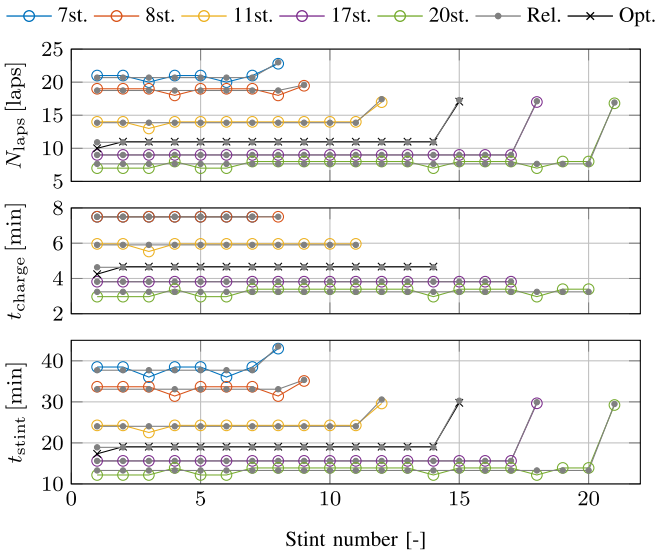

Fig. 17. Optimal race strategy (black) in terms of stint length, charge, and stint time with $t_{\text{charge,max}} = 7.5$ min. For comparison, we show other optimal fixed pit stop strategies together with the relaxed solution in gray. Stint length, charge, and stint time are related and the optimal integer solution minimizes the differences from the relaxed solution.

optimal stint, thereby highlighting the importance of jointly optimizing the stint lengths, charge times, and number of pit stops. Finally, to show the importance of the bi-level approach, we compare the optimal strategy against a baseline *flat-out* strategy whereby no energy management is applied to limit energy consumption, but the EMs are operated at maximum power whenever possible. This results in 6 lap stints and a total race distance of 132 laps, whilst the globally optimal solution is about 170 laps. Hence, the optimal solution is about 29% better compared to the baseline, even though the baseline was computed without thermal limits.

Fig. 17 shows the individual stints in terms of length and charge time, together with the relaxed noninteger solution. We can conclude that a constant stint length over the race is optimal since all stints in the relaxed solutions are equal, the only exception being the last stints. In this use case, the optimal integer solution consists of the stint lengths that minimize the difference to the relaxed solution, namely, of a stint length between 10 and 11 laps together with a charge time of about 4.7 min and 14 pit stops in total. For the vehicle considered in this study, the 8 stop strategy is the fastest strategy that involves fully charging the battery. However, this strategy is 0.6 laps behind on the optimal race strategy, thereby showing that fully charging the battery can be suboptimal. This is explained by the constant current charging, which effectively reduces the average charging power for longer charge times due to the battery voltage decreasing for lower energy levels. With a different charging profile, such as constant power charging, a different optimal race strategy will be obtained. However, it is beyond the scope of this article to optimize the charging profile. Moreover, reducing the charge time results in shorter stints, thereby increasing the number of pit stops needed, as indicated by the results. This then results in more time lost in the pit lane due to the speed limit. Thus, there is a clear tradeoff in determining the optimal charge time. When we also consider thermally-limited scenarios, this tradeoff becomes even more complex. In these cases, a shorter charge time is expected to be in favor, since this increases the terminal battery temperature. Although a longer charge time reduces the initial EM temperature, we observed that this had a relatively small impact on the stint time. In fact, it has been observed that in longer stints the EM was operated relatively more at the thermal limit compared to shorter stints, thereby disfavoring longer charge times. Finally, we observe that there is a considerable decrease in race distance when an increasing stint length cannot be compensated by an increase in charge time, as illustrated by the difference between the 7- and 8-stop strategies. From the aforementioned observations, we conclude that the stint length, stint time, and charge time are closely related in the case of an optimal solution.

C. Validation

In this section, we validate the correctness of the model by showing that the lethargy constraint holds equality for various stints that were presented in the previous section. Furthermore, we validate the convex models by implementing the optimal inputs into a nonlinear simulator and compare the drift in battery energy. Finally, we validate the numerical combinations of stint length and charge time for the various strategies. For the latter, we calculate the average stint velocity $\overline{v}_{\text{stint}}(k)$ for every strategy as

$$\overline{v}_{\text{stint}}(k) = \frac{S_{\text{stint}}(k)}{t_{\text{charge}}(k) + t_{\text{stint}}(k)} \quad \forall k \in \left[0, n_{\text{stops}} - 1\right]. \tag{78}$$

The globally optimal stint should maximize the average stint velocity since that maximizes the driven distance per unit of time, also accounting for the charge time after the stint. We can calculate the average stint velocity for various combinations of stint length and charge time using the

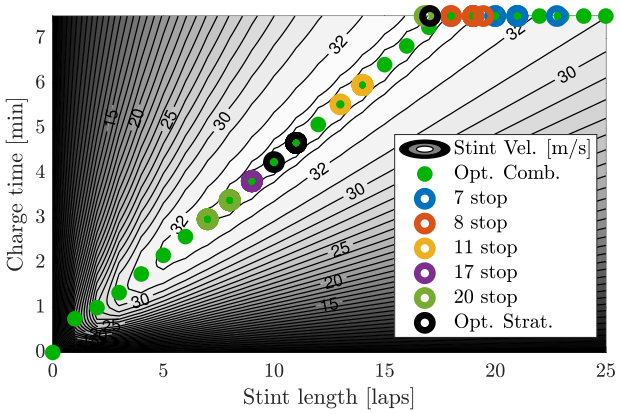

Fig. 18. Average stint velocity for a combination of stint lengths and charge times together with the optimal combinations and actual numerical solutions. The optimal combinations of stint length and charge time show a clear (linear) correlation, to which the numerical solutions are aligned.

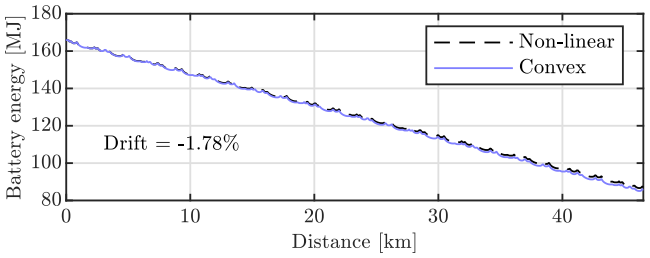

Fig. 19. Battery energy calculated through the nonlinear and convex models, using the optimized inputs for the globally optimal stint of 11 laps and 4.7 min charging. The small drift in battery energy between the nonlinear and convex models indicates that the convex models accurately capture the dynamics of the powertrain components.

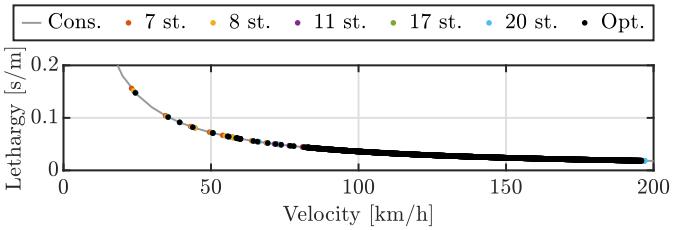

Fig. 20. Validation of the lethargy constraint for the mode of the stints obtained from the high-level optimization. All data points align with the constraint (within the solver tolerance), indicating that the lethargy constraint holds with equality.

stint time map. To validate the correctness of the optimized strategies, we calculate the optimal charge time that maximizes the average stint velocity, for every possible stint length. These are referred to as the optimal combinations of charge times and stint length. The optimized strategies should align with these theoretical optimal combinations when looking from a stint perspective. However, small deviations might be observed, since the strategies are optimized from a race perspective. Fig. 18 shows the average stint velocity together with the theoretical optimal combinations. These optimal combinations indicate an almost linear relation between charge time and stint length until the maximum charge time is reached. The most noticeable exception is the single-lap stint, which has a relatively higher optimal charge time. This is because a single-lap stint does not include a flying lap, where the vehicle starts the lap with a high initial velocity. Thus, the vehicle requires more energy in the first lap to accelerate toward the optimal velocity, which explains the longer charge time for a single-lap stint. The globally optimal stint with the highest average stint velocity consists of 11 laps and 4.7 min charging, which is the exact same combination that we obtained as the optimal strategy in the previous section. Furthermore, we observe that the average stint velocity decreases in sensitivity around the optimal combinations for increasing stint length and charge time. When the maximum charge time is reached, the average stint velocity diminishes considerably for increasing stint lengths. Thereby, increasing the stint length beyond 18 laps quickly becomes less favorable, since it cannot be compensated by an increase in charge time. This explains why the 7 stop strategy is significantly worse than the others. Finally, we note that the numerical solutions are in line with the theoretically optimal combinations, thereby validating their correctness. The outliers not aligning with the optimal combinations, e.g., at 16.8 laps and 7.5 min charging, correspond to the last stints, for which the charge time is not part of the race and thus the calculation of the stint velocity in (78) is not valid.

To validate the convex loss models for the EM and battery, we calculate the battery energy trajectory by applying the optimal input trajectories to nonlinear models and compare the result to the trajectory obtained from the optimization. Fig. 19 shows both battery energy trajectories for the globally optimal stint of 11 laps with 4.7 min charging. From this figure, we observe small deviations, with a total drift of -1.78 % with respect to the nonlinear models, thereby indicating that the convex models accurately capture the dynamics of the powertrain components.

Finally, we verify that all relaxed constraints hold with equality. As noted previously, it can occur that the lethargy constraint does not hold with equality in thermally-limited scenarios. Therefore, we explicitly show this constraint for the most frequently used stints per pit stop strategy that were obtained in the previous section. Fig. 20 shows that all data points align with the constraint, thereby indicating that the lethargy constraint holds with equality for all optimal stints.

VI. Conclusion

In this article, we studied the maximum-distance endurance racing problem for electric race cars, explicitly accounting for temperature and vehicle dynamics. To this end, we devised a convex bi-level optimization framework that can efficiently compute the optimal race strategy (in terms of stint lengths, charge times, and pit stops), jointly with the in-stint PO strategy.

Our results showed that accounting for the temperature dynamics of the powertrain components is extremely important in an endurance racing scenario and that both the in-stint PO and the high-level race strategy were affected by it. From a stint perspective, there is a clear correlation between optimal stint length and charge time, which corresponds to the maximization of the average stint velocity. In contrast to our preliminary results [25], fully charging the battery proved to be suboptimal for this case study, because increasing the

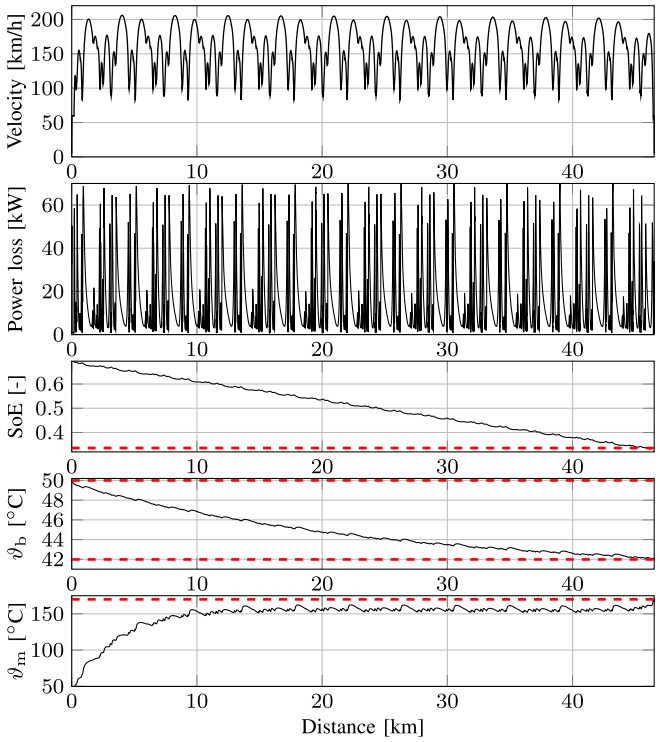

Fig. 21. Velocity, powertrain losses, battery SoE, battery temperature, and EM temperature trajectories for an 11-lap stint. The terminal battery temperature is an active constraint, which results in a gradual decrease in battery temperature throughout the stint to allow for some margin in temperature for the consecutive charging session.

battery operating window results in a lower average charge power and stricter battery temperature limitations. Moreover, the results suggest avoiding the usage of mechanical friction brakes, which indicates the paramount importance of efficient energy management for electric race cars. In fact, this highlights the shortcomings and need for improvement of current battery technologies, compared to hybrid-electric vehicles in racing scenarios. Finally, we highlighted the importance of optimizing both levels by showing that a repetition of the optimal stint does not result in an optimal race.

This work opens the field for the following possible extensions. First, we are interested in the impact of tire degradation and temperature on the achievable stint time and the resulting race strategies, since this yields an apparent tradeoff with energy management. Second, we want to extend the usage of the framework to an investigation of the optimal transmission technology and powertrain architecture. Finally, we would like to leverage the computational efficiency of the framework for an online implementation both in the vehicle, as well as in the pit lane.

APPENDIX

In Section II-E, we frequently used the following relaxations

$$x \cdot y \geq z^\top z \tag{79}$$

which defines a convex set. To prove convexity, we can rewrite this constraint to a convex second-order conic constraint as

$$x + y \geq \left\| \begin{matrix} 2 \cdot z \\ x - y \end{matrix} \right\|_2 \tag{80}$$

which can be solved with global optimality guarantees [33]. Since (79) is mathematically equivalent to (80), both optimization problems will converge to the same KKT points, thereby guaranteeing global optimality.

Another type of constraint that was used in Section II-E for the friction circles is

$$x^2 + y^2 \leq z^2. \tag{81}$$

This constraint can be directly translated to a convex second-order conic constraint

$$\left\| \begin{matrix} x \\ y \end{matrix} \right\|_2 \leq z \tag{82}$$

thereby proving that (81) defines a convex set.

In Section V-A, we mentioned that an active terminal battery temperature constraint results in a gradual decrease in battery temperature over the entire stint. Fig. 21 again shows an 11 lap stint, but with increased thermal resistance for the battery, thereby resulting in an active battery temperature constraint. Comparing this figure to Fig. 14, we can clearly see the difference in battery temperature trajectories. Whereas the battery temperature was kept close to the maximum before to maximize the efficiency, the temperature is now gradually decreasing to reach the required terminal value.

ACKNOWLEDGMENT

The authors thank Dr. I. New for proofreading this article, and N. Schoenmakers for the photograph of the car shown in Fig. 1.

REFERENCES

[1] InMotion. (2023). *InMotion Fully Electric LMP3 Car*. [Online]. Available: https://www.inmotion.tue.nl/en/about-us/cars/revolution

[2] FIA. (2021). *2021 FIA World Endurance Championship: Sporting Regulations*. [Online]. Available: https://www.fia.com/sites/default/files/2021_wec_sporting_regulations_-_wmsc161220-clean_1.pdf

[3] R. Lot and S. Evangelou, "Lap time optimization of a sports series hybrid electric vehicle," in *Proc. World Congr. Eng.*, 2013, pp. 1–12.

[4] T. Sedlacek, D. Odenthal, and D. Wollherr, "Minimum-time optimal control for battery electric vehicles with four wheel-independent drives considering electrical overloading," *Vehicle Syst. Dyn.*, vol. 60, no. 2, pp. 491–515, Feb. 2022.

[5] D. Casanova, "On minimum time vehicle manoeuvring: The theoretical optimal lap," Ph.D. dissertation, School Eng., Cranfield Univ., Cranfield, U.K., 2000.

[6] G. Perantoni and D. J. N. Limebeer, "Optimal control for a formula one car with variable parameters," *Vehicle Syst. Dyn.*, vol. 52, no. 5, pp. 653–678, May 2014.

[7] F. Christ, A. Wischnewski, A. Heilmeier, and B. Lohmann, "Time-optimal trajectory planning for a race car considering variable tyre-road friction coefficients," *Vehicle Syst. Dyn.*, vol. 59, no. 4, pp. 588–612, Apr. 2021.

[8] N. Dal Bianco, R. Lot, and M. Gadola, "Minimum time optimal control simulation of a GP2 race car," *Proc. Inst. Mech. Eng., D, J. Automobile Eng.*, vol. 232, no. 9, pp. 1180–1195, Aug. 2018.

[9] A. Heilmeier, A. Wischnewski, L. Hermansdorfer, J. Betz, M. Lienkamp, and B. Lohmann, "Minimum curvature trajectory planning and control for an autonomous race car," *Vehicle Syst. Dyn.*, vol. 58, no. 10, pp. 1497–1527, Oct. 2020.

[10] M. Massaro and D. J. N. Limebeer, "Minimum-lap-time optimisation and simulation," *Vehicle Syst. Dyn.*, vol. 59, no. 7, pp. 1069–1113, Jul. 2021.

[11] A. J. Tremlett and D. J. N. Limebeer, "Optimal tyre usage for a formula one car," *Vehicle Syst. Dyn.*, vol. 54, no. 10, pp. 1448–1473, Oct. 2016.

[12] T. Herrmann, F. Christ, J. Betz, and M. Lienkamp, "Energy management strategy for an autonomous electric racecar using optimal control," in *Proc. IEEE Intell. Transp. Syst. Conf. (ITSC)*, Oct. 2019, pp. 720–725.

[13] D. J. N. Limebeer, G. Perantoni, and A. V. Rao, "Optimal control of formula one car energy recovery systems," *Int. J. Control*, vol. 87, no. 10, pp. 2065–2080, 2014.
[14] T. Herrmann, F. Passigato, J. Betz, and M. Lienkamp, "Minimum race-time planning-strategy for an autonomous electric racecar," in *Proc. IEEE 23rd Int. Conf. Intell. Transp. Syst. (ITSC)*, Sep. 2020, pp. 1–6.
[15] X. Liu, A. Fotouhi, and D. J. Auger, "Optimal energy management for formula-E cars with regulatory limits and thermal constraints," *Appl. Energy*, vol. 279, Dec. 2020, Art. no. 115805.
[16] T. Herrmann, F. Sauerbeck, M. Bayerlein, J. Betz, and M. Lienkamp, "Optimization-based real-time-capable energy strategy for autonomous electric race cars," *SAE Int. J. Connected Automated Vehicles*, vol. 5, no. 1, pp. 45–59, Jan. 2022.
[17] X. Liu and A. Fotouhi, "Formula-E race strategy development using artificial neural networks and Monte Carlo tree search," *Neural Comput. Appl.*, vol. 32, no. 18, pp. 15191–15207, Sep. 2020.
[18] S. Ebbesen, M. Salazar, P. Elbert, C. Bussi, and C. H. Onder, "Time-optimal control strategies for a hybrid electric race car," *IEEE Trans. Control Syst. Technol.*, vol. 26, no. 1, pp. 233–247, Jan. 2018.
[19] M. Salazar, P. Elbert, S. Ebbesen, C. Bussi, and C. H. Onder, "Time-optimal control policy for a hybrid electric race car," *IEEE Trans. Control Syst. Technol.*, vol. 25, no. 6, pp. 1921–1934, Nov. 2017.
[20] P. Duhr, G. Christodoulou, C. Balerna, M. Salazar, A. Cerofolini, and C. H. Onder, "Time-optimal gearshift and energy management strategies for a hybrid electric race car," *Appl. Energy*, vol. 282, Jan. 2021, Art. no. 115980.
[21] O. Borsboom, C. A. Fahdzyana, T. Hofman, and M. Salazar, "A convex optimization framework for minimum lap time design and control of electric race cars," *IEEE Trans. Veh. Technol.*, vol. 70, no. 9, pp. 8478–8489, Sep. 2021.
[22] A. Locatello, M. Konda, O. Borsboom, T. Hofman, and M. Salazar, "Time-optimal control of electric race cars under thermal constraints," in *Proc. Eur. Control Conf. (ECC)*, Jun. 2021, pp. 905–912.
[23] A. Heilmeier, M. Graf, and M. Lienkamp, "A race simulation for strategy decisions in circuit motorsports," in *Proc. 21st Int. Conf. Intell. Transp. Syst. (ITSC)*, Nov. 2018, pp. 1–11.
[24] W. J. West and D. J. N. Limebeer, "Optimal tyre management for a high-performance race car," *Vehicle Syst. Dyn.*, vol. 60, no. 1, pp. 1–19, Jan. 2022.
[25] J. van Kampen, T. Herrmann, and M. Salazar, "Maximum-distance race strategies for a fully electric endurance race car," *Eur. J. Control*, vol. 68, Nov. 2022, Art. no. 100679.
[26] S. Broere, J. Van Kampen, and M. Salazar, "Minimum-lap-time control strategies for all-wheel drive electric race cars via convex optimization," in *Proc. Eur. Control Conf. (ECC)*, Jul. 2022, pp. 1204–1211.
[27] L. Guzzella and A. Sciarretta, *Vehicle Propulsion Systems: Introduction to Modeling and Optimization*, 2nd ed. Berlin, Germany: Springer, 2007.
[28] O. Borsboom, C. A. Fahdzyana, and M. Salazar, "Time-optimal control strategies for electric race cars with different transmission technologies," in *Proc. IEEE Vehicle Power Propuls. Conf. (VPPC)*, Nov. 2020, pp. 296–300.
[29] R. Zhang et al., "A study on the open circuit voltage and state of charge characterization of high capacity lithium-ion battery under different temperature," *Energies*, vol. 11, no. 9, p. 2408, Sep. 2018.
[30] A. Farmann and D. U. Sauer, "A study on the dependency of the open-circuit voltage on temperature and actual aging state of lithium-ion batteries," *J. Power Sources*, vol. 347, pp. 1–13, Apr. 2017.
[31] D. M. Rosewater, D. A. Copp, T. A. Nguyen, R. H. Byrne, and S. Santoso, "Battery energy storage models for optimal control," *IEEE Access*, vol. 7, pp. 178357–178391, 2019.
[32] A. Łebkowski, "Temperature, overcharge and short-circuit studies of batteries used in electric vehicles," *Przegld Elektrotechniczny*, vol. 1, no. 5, pp. 69–75, May 2017.
[33] S. Boyd and L. Vandenberghe, *Convex Optimization*. Cambridge, U.K.: Cambridge Univ. Press, 2004.
[34] A. Richards and J. How, "Mixed-integer programming for control," in *Proc. Amer. Control Conf.*, 2005, pp. 2676–2683.
[35] J. Lee and S. Leyffer, *Mixed Integer Nonlinear Programming*. Cham, Switzerland: Springer-Verlag, 2012.
[36] P. Belotti, C. Kirches, S. Leyffer, J. Linderoth, J. Luedtke, and A. Mahajan, "Mixed-integer nonlinear optimization," *Acta Numerica*, vol. 22, pp. 1–131, May 2013.
[37] J. A. E. Andersson, J. Gillis, G. Horn, J. B. Rawlings, and M. Diehl, "CasADi: A software framework for nonlinear optimization and optimal control," *Math. Program. Comput.*, vol. 11, no. 1, pp. 1–36, Mar. 2019.
[38] A. Wächter and L. T. Biegler, "On the implementation of an interior-point filter line-search algorithm for large-scale nonlinear programming," *Math. Program.*, vol. 106, no. 1, pp. 25–57, Mar. 2006.
[39] HSL. *A Collection of Fortran Codes for Large Scale Scientific Computation*. Accessed: Nov. 3, 2021. [Online]. Available: http://www.hsl.rl.ac.uk
[40] J. Lofberg, "YALMIP: A toolbox for modeling and optimization in MATLAB," in *Proc. IEEE Int. Conf. Robot. Autom.*, Jan. 2004, pp. 284–289.
[41] (2017). *MOSEK Optimization Software*. [Online]. Available: https://mosek.com/
[42] S. Lovato and M. Massaro, "A three-dimensional free-trajectory quasi-steady-state optimal-control method for minimum-lap-time of race vehicles," *Vehicle Syst. Dyn.*, vol. 60, no. 5, pp. 1512–1530, May 2022.

Jorn van Kampen received the B.Sc. (Hons.) and M.Sc. (cum laude) degrees in automotive technology from the Eindhoven University of Technology (TU/e), Eindhoven, The Netherlands, in 2018 and 2022, respectively, where he is currently pursuing the Ph.D. degree with the Control Systems Technology Section.

His main research interests include electric race vehicles and optimization methods for powertrain design and control.

Mr. van Kampen was granted the Best Student Paper Award at the 2022 European Control Conference and the master's thesis received the 2022 Tata Steel Graduation Award for Mechanical Engineering and Material Science.

Thomas Herrmann received the B.Sc. and M.Sc. degrees in mechanical engineering from the Technical University of Munich (TUM), Munich, Germany, in 2016 and 2018, respectively, and the Ph.D. degree from the Institute of Automotive Technology, TUM, in 2022.

His research interests include optimal control in the field of trajectory planning for autonomous vehicles and the efficient incorporation of electric powertrain behavior within these optimization problems.

Dr. Herrmann was granted the Best Student Paper Award at the 2022 European Control Conference.

Theo Hofman was born in Utrecht, The Netherlands, in 1976. He received the M.Sc. (Hons.) and Ph.D. degrees in mechanical engineering from the Eindhoven University of Technology, Eindhoven, The Netherlands, in 1999 and 2007, respectively.

From 1999 to 2003, he was a Researcher and a Project Manager with the Research and Development Department, Thales-Cryogenics B.V., Eindhoven. From 2003 to 2007, he was a Scientific Researcher with Drivetrain Innovations B.V., Eindhoven. Since 2010, he has been an Associate Professor with the Control Systems Technology Group. His research interests include system design optimization methods for complex dynamical engineering systems and discrete topology design using computational design synthesis.

Mauro Salazar received the Ph.D. degree in mechanical engineering from ETH Zürich, Zürich, Switzerland, in 2019.

He is currently an Assistant Professor with the Control Systems Technology Section, Eindhoven University of Technology (TU/e), Eindhoven, The Netherlands, and co-affiliated with the Eindhoven AI Systems Institute (EAISI). Before joining TU/e, he was a Post-Doctoral Scholar with the Autonomous Systems Laboratory, Stanford University, Stanford, CA, USA. His research interests include optimization models and methods for cyber-socio-technical systems design and control, with a strong focus on sustainable mobility.

Dr. Salazar's master's and Ph.D. thesis were recognized with the ETH Medal and his papers were granted the Best Student Paper Awards at the 2018 Intelligent Transportation Systems Conference and at the 2022 European Control Conference.